Harmonic Nanocrystals for Biolabeling: A Survey of Optical Properties and Biocompatibility

Davide Staedler,[†] Thibaud Magouroux,[‡] Rachid, Hadji,[§] Cécile Joulaud,[§] Jérôme Extermann,[‡] Sebastian Schwung,[⊥] Solène Passemard,[†] Christelle Kasparian,[‡] Gareth Clarke,[§] Mathias Gerrmann,[⊥] Ronan Le Dantec,[§] Yannick Mugnier,[§] Daniel Rytz,[⊥] Daniel Ciepielewski,[∥] Christine Galez,[§] Sandrine Gerber-Lemaire,[†] Lucienne Juillerat-Jeanneret,[#] Luigi Bonacina,[‡,*] and Jean-Pierre Wolf[‡]

[†]Laboratory of Synthesis and Natural Products, Institute of Chemical Sciences and Engineering, École Polytechnique Fédérale de Lausanne, Batochime, 1015 Lausanne, Switzerland, [‡]GAP-Biophotonics, Université de Genève, 22 Chemin de Pinchat, 1211 Genève 4, Switzerland, [§]SYMME, Université de Savoie, BP 80439, 74944, Annecy Le Vieux Cedex, France, [⊥]FEE Gmbh, Struthstrasse 2, 55743 Idar-Oberstein, Germany, [∥]Nikon France, Division Instruments, 191 Rue du Marché Rollay, 94504 Champigny Sur Marne Cedex, France, and [#]Centre Hospitalier Universitaire Vaudois and Institute of Pathology, University of Lausanne, Rue du Bugnon 25, 1011 Lausanne, Switzerland

ABSTRACT

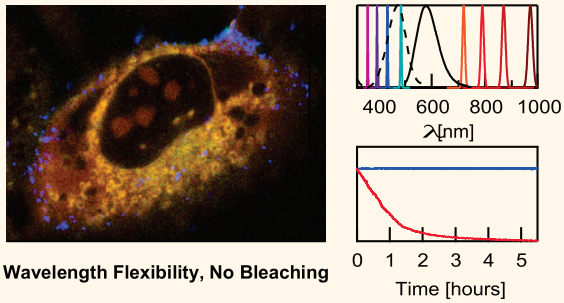

Nonlinear optical nanocrystals have been recently introduced as a promising alternative to fluorescent probes for multiphoton microscopy. We present for the first time a complete survey of the properties of five nanomaterials ($KNbO_3$, $LiNbO_3$, $BaTiO_3$, KTP, and ZnO), describing their preparation and stabilization and providing quantitative estimations of their nonlinear optical response. In the light of their prospective use as biological and clinical markers, we assess their biocompatibility on human healthy and cancerous cell lines. Finally, we demonstrate the great potential for cell imaging of these inherently nonlinear probes in terms of optical contrast, wavelength flexibility, and signal photostability.

KEYWORDS: harmonic nanoparticles · nonlinear microscopy · cell labeling

The development of imaging labels for microscopy has followed some unexpected routes in the past decade. Superresolution techniques based on stochastic intensity fluctuations have redefined the very requirements on fluorophores, shifting the focus to the possibility of photoactivation and dark states lifetimes rather than stability against bleaching.[1] On the other hand, the diffusion of nonlinear microscopy systems[2] based on tunable Ti:Sapphire laser sources, thanks to their intrinsic 3D sectioning capability, has raised the demand for photostable fluorophores with two-photon absorption bands in the near-infrared (to limit sample degradation and increase penetration depth) and narrow emission bands (to better distinguish them from autofluorescence background). Very recently, to complement the development of fluorescence-based labels (dyes, quantum dots, up-converting nanoparticles[3]), a completely different approach has appeared promoting the use of a novel family of inherently nonlinear nanoparticles (NPs), specifically conceived for multiphoton microscopy.[4] These labels, based on inorganic noncentrosymmetric crystals, exert an optical contrast mechanism by second harmonic (SH) generation of the excitation frequency: for example, converting a fraction of near-infrared pulsed excitation light (800 nm) into visible blue light (400 nm). Compared to fluorescent probes, they possess a series of attractive properties, including complete absence of bleaching and blinking,[5] narrow emission bands, excitation-wavelength tunability,[6,7] orientation retrieval capability,[4,8,9] and coherent optical response.[10−13] So far, what we believe is the immense imaging potential of their coherent emission has not been fully exploited, and just a few demonstration measurements have been published on specially conceived setups.[10,14,13] On the other hand, the possibility to work in the infrared range with an infinitely photostable signal clearly makes them readily amenable

* Address correspondence to luigi.bonacina@unige.ch.

Received for review December 20, 2011 and accepted February 10, 2012.

Published online February 10, 2012
10.1021/nn204990n

for long-term cell tracking with commercial nonlinear microscopes.

In this work we perform a systematic screening of most of the nonlinear nanomaterials proposed so far in the literature: potassium niobate ($KNbO_3$),[15] lithium niobate ($LiNbO_3$),[16] barium titanate ($BaTiO_3$),[14,17] potassium titanyl phosphate ($KTiOPO_4$, KTP),[11,13] and zinc oxide (ZnO).[18,19] We specifically address the properties of polyethylene glycol (PEG)-stabilized suspensions of these harmonic nanoparticles (HNPs). For the first time, we compare their ensemble nonlinear optical properties in terms of SH generation efficiency and chemical stability in aqueous solution at biological pH. We then assess their cytotoxicity on several human cancerous and healthy cell lines derived from lung. In conclusion, we discuss their performance in terms of multiphoton imaging. Such a thorough comparison is meant to allow identifying the SH nanomaterial with the best performances for future biomedical imaging applications.

RESULTS AND DISCUSSION

Nanoparticle Colloidal Stabilization. The preparation protocol applied to all HNPs under scrutiny is detailed in the Materials and Methods section. This procedure was found to be very reproducible for $LiNbO_3$ and $KNbO_3$. Conversely, the results for ZnO, KTP, and $BaTiO_3$ were far less reliable in particular for the sonication and sedimentation steps, and repeated measurements did not yield consistent results. A higher polydispersity in the raw powder (as shown in the transmission electron microscope (TEM) images in the Supporting Information) together with the presence of agglomerates could account for such a poor reliability for these three nanomaterials. Table 1 summarizes the decantation time and the mean size distribution by number retrieved by dynamic light scattering (DLS) of HNP suspensions before adding PEG, and after adding PEG and performing the final centrifugation. For all the HNPs, the improved colloidal stability after PEG adsorption was confirmed by the easy redispersion of centrifuged powders in deionized water. For $LiNbO_3$ and $KNbO_3$, a systematic 10−20 nm shift was observed in the DLS size distribution by number (see Supporting Information), which can be attributed to a noncovalent wrapping of HNPs with PEG. Moreover, PEG addition also led to a systematic 5−10 mV decrease in the zeta-potential absolute values, in agreement with previous studies on oxide nanoparticles.[20,21] Finally, a Fourier transform infrared (FTIR) analysis was performed on $KNbO_3$ HNPs after centrifugation. In the infrared spectra (see Supporting Information), all vibrational bands of PEG could be identified, confirming the previous observations.

Second-Order Nonlinear Optical Efficiency of Nanocrystals. To assess the SH generation efficiency of the different nanomaterials, we performed a systematic series of hyper-Rayleigh scattering (HRS) measurements on HNP suspensions. This approach[22] leads to the determination of the squared hyperpolarizability averaged over all possible NP orientations, $\langle\beta_{np}^2\rangle$. Neglecting solvent contributions, the SH intensity, $I_{2\omega}$, can be expressed as

$$I_{2\omega} = G(N_{np}T_{np}\langle\beta_{np}^2\rangle)I_{\omega}^2$$

where G is an experimental proportionality constant, N_{np} the HNP concentration, and T_{np} the reduction field factor due to the refractive index change between water and HNPs. After calibrating the experimental setup by the external reference method,[23] we derived quantitative $\langle\beta_{np}^2\rangle$ values for a vertical polarization of the incident laser and no polarization analyzer in front of the detection. The $\langle\beta_{np}\rangle$ values reported in Table 2 can be directly related to the averaged bulk nonlinear coefficient $\langle d\rangle$ by $\langle\beta_{np}\rangle = \langle d\rangle V_{np}$, where V_{np} is the HNP volume.[22,24] As the HRS signal scales with the square of the particle volume, the normalized hyperpolarizability $\langle d\rangle = \langle\beta_{np}\rangle/V_{np}$ is also reported in Table 2 to allow a direct comparison of the nonlinear efficiency of the different nanomaterials tested. The $\langle\beta_{np}\rangle$ values retrieved are large with respect to typical molecular hyperpolarizabilities, pointing at the good nonlinear optical efficiency of the HNPs. These results confirm previous measurements on $BaTiO_3$,[25] and they constitute the first experimental hyperpolarizabilities obtained at the nanoscale for all the other materials.

An important source of error when determining $\langle\beta\rangle$ and $\langle d\rangle$ is related to the difficulty of evaluating individual NP sizes by DLS, mainly because of the broad size

TABLE 1. Decantation Time (t_D) and Mean DLS Size (Size Distribution by Number) for Different HNPs (a) before PEG Addition and (b) after Centrifugation

nanocrystal	t_D [days]	DLS (a) [nm]	DLS (b) [nm]
$KNbO_3$	7	123	132
$LiNbO_3$	7	113	122
$BaTiO_3$	1	119	123
KTP	2	119	196
ZnO	7	133	110

TABLE 2. Hyperpolarizability $\langle\beta_{np}\rangle$, Normalized Hyperpolarizability $\langle d\rangle$, and Normalized Hyperpolarizability from Bulk Materials Found in Literature $\langle d_{lit.}\rangle$ of $KNbO_3$, $LiNbO_3$, $BaTiO_3$, KTP, and ZnO Nanocrystals

nanocrystal	$\langle\beta_{np}\rangle \pm \Delta\beta$ ($\times 10^{-24}$ esu)	$\langle d_{np}\rangle \pm \Delta d$, pm/V	$\langle d_{lit}\rangle$, pm/V
$KNbO_3$	7.2 ± 2.4	3.4 ± 1.1	15.3
$LiNbO_3$	21 ± 7.0	4.8 ± 1.6	17.3
$BaTiO_3$	11.0 ± 3.5	4.6 ± 0.7	14.1
KTP	25.8 ± 6.0	1.4 ± 0.3	7.6
ZnO	9.6 ± 2.8	1.9 ± 0.6	2.8

distribution and the presence of aggregates in suspension.[22] Being aware of this problem, we proceeded in a systematic inspection of the suspensions prior to HRS measurement, obtaining reproducible results and a correct agreement retrieved between experimental $\langle d_{np} \rangle$ and calculated $\langle d_{bulk} \rangle$ values. The latter are deduced from the literature values of the d_{ij} tensor elements, which range from $\langle d_{bulk} \rangle = 2.8$ for ZnO to $\langle d_{bulk} \rangle = 17.3$ for $LiNbO_3$. Our results confirm the absence of a size effect in the SH properties and the bulk origin of the nonlinear signal detected, in agreement with the relatively large size of the HNPs. Furthermore, we point out here that the nonlinear optical efficiencies of the different materials are relatively similar. Consistently with previous microscopy experiments on isolated HNPs, the SH intensity appeared to be more significantly affected by the HNP volume (with a squared intensity dependence) and orientation[4,8,5] than by the material itself.

Biological Assays. We carried out a thorough biological evaluation of HNPs, including cytotoxicity and hemolysis assays. Possible microbial contamination in the HNP stock solutions and solutions of HNPs at 50 μg/mL in the different culture media were tested in order to avoid interference in cellular assays due to the presence of bacteria or fungi. Only weak contaminations in the stock solutions of $KNbO_3$ (100 bacteria/mL) and of KTP (300 bacteria/mL) were detected, but no contaminations were observed for HNPs in cell culture media in the presence of antibiotics (streptavidin/penicillin).

HNP Cytotoxicity. The viability of cells exposed to different HNPs was assessed by the MTT (3-(4,5-dimethyl-2-thiazoyl)-2,5-diphenyltetrazolium bromide) test. As a preliminary check, HNPs were tested for interferences, as it is known that NPs can deplete MTT in solutions, can catalyze MTT reduction, and may directly influence the readout by increasing light absorption.[26] The absence of interference by both uncoated and PEG-stabilized HNPs at 50 and 100 μg/mL was verified by reading the absorbance of the HNP solutions at 540 nm and by adding MTT directly in the HNP solutions for 5, 24, or 72 h. The MTT test was then applied on three human lung cancer cell lines, one human adenocarcinoma cell line (A549) derived from alveolar epithelial type II cells, one adenosquamos carcinoma cell line (HTB-178), and one lung squamous carcinoma cell line (HTB-182).[27−29] Moreover, we also tested nontumoral BEAS-2B cells. The latter are a subclone of transformed adult human bronchial epithelial cells that express phenotypic characteristics of nonciliated mucus-secreting epithelial cells.[30] The cytotoxicity of HNPs was then measured at 10, 50, and 100 μg/mL. Lung-derived cell survival at 50 μg/mL is reported in Table 3. $KNbO_3$ and $LiNbO_3$ HNPs show a weak cytotoxicity in all the samples after 5 or 24 h exposure. $BaTiO_3$ was found to be the least cytotoxic among the nanomaterials tested, its cytotoxicity being comparable among the four cell lines under consideration. Globally, HNPs at 50 μg/mL cause a 20−30% decrease in cell survival in the majority of the cell lines tested, leaving a sufficiently high number of living cells for performing cellular assays and biological evaluations. KTP caused a time-dependent decrease in cell survival in all cell lines, an effect even more pronounced in nontumoral BEAS-2B cells. Conversely, cell exposure to ZnO HNPs was found highly cytotoxic, already after 5 h incubation. On the ground of these results, KTP HNPs were excluded from further biological evaluations because of their instability in suspension and ZnO HNPs because of their high cytotoxicity. The effects on cell survival after 72 h exposure of $KNbO_3$, $LiNbO_3$, and $BaTiO_3$ NPs at 50 μg/mL are shown in the last row of Table 3. One can notice that none of these HNPs show major effects on cell survival even after such a long exposure.

TABLE 3. Cytotoxic Effect after 5, 24 or 72 h Exposure of Human Lung-Derived Cells to $KNbO_3$, $LiNbO_3$, $BaTiO_3$, KTP, and ZnO Nanoparticles (50 μg/mL)[a]

	% of surviving cells				
5 h	$KNbO_3$	$LiNbO_3$	$BaTiO_3$	KTP	ZnO
A549	81.2 ± 4.4	78.6 ± 3.7	91.0 ± 5.3	76.3 ± 4.2	57.7 ± 7.8
HTB-182	81.6 ± 6.7	82.6 ± 2.7	87.1 ± 9.4	67.8 ± 2.3	41.6 ± 7.8
HTB-178	74.3 ± 2.1	90.7 ± 8.8	87.7 ± 12.7	78.4 ± 6.2	27.8 ± 6.7
BEAS-2B	84.9 ± 5.3	87.9 ± 7.1	93.1 ± 0.6	63.2 ± 5.6	29.9 ± 6.7
24 h	$KNbO_3$	$LiNbO_3$	$BaTiO_3$	KTP	ZnO
A549	82.0 ± 3.6	84.7 ± 5.7	84.7 ± 3.8	67.8 ± 2.5	17.7 ± 5.3
HTB-182	73.7 ± 6.7	80.9 ± 3.5	85.5 ± 1.3	61.4 ± 6.0	4.5 ± 1.0
HTB-178	74.2 ± 1.0	83.6 ± 3.3	91.8 ± 1.7	76.8 ± 7.7	6.8 ± 1.2
BEAS-2B	81.7 ± 4.0	93.9 ± 4.9	92.1 ± 3.7	55.8 ± 5.3	9.9 ± 3.3
72 h	$KNbO_3$	$LiNbO_3$	$BaTiO_3$	KTP	ZnO
A549	69.8 ± 4.1	73.5 ± 5.2	81.4 ± 8.2	NA	NA
HTB-182	77.4 ± 4.5	80.5 ± 5.5	88.9 ± 2.3	NA	NA
HTB-178	56.9 ± 5.7	81.9 ± 6.5	74.5 ± 9.1	NA	NA
BEAS-2B	64.4 ± 4.9	70.9 ± 4.3	78.2 ± 9.1	NA	NA

[a] A549, HTB-182, and HTB-178: human lung cancer cells; BEAS-2B: nontumoral lung-derived cells. Results are the mean ± SD of triplicates of two independent experiments.

Hemolytic Properties of the NPs. Hemolysis is defined as the destruction of red blood cells, and *in vivo* it can cause several pathological conditions. Hemolytic effects of NPs may be due to electrostatic interactions between NPs and membrane proteins or by other NP-specific mechanisms, such as generation of reactive oxygen species. Although this assay is not often performed, we found it of paramount importance to characterize the hemolytic behavior of HNPs in order to ensure that they can be used for future clinical applications. The hemolytic effect of PEG-stabilized $KNbO_3$, $LiNbO_3$, and $BaTiO_3$ HNPs was determined at

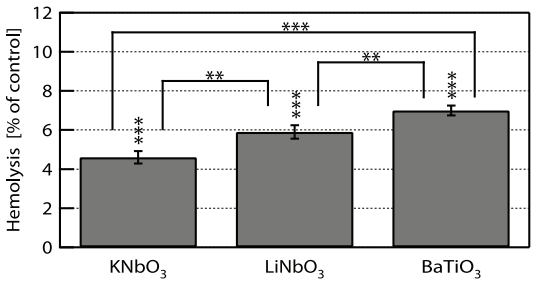

Figure 1. Hemolytic effect in human red blood cells exposed for 2 h to $KNbO_3$, $LiNbO_3$, and $BaTiO_3$ nanoparticles (50 μg/mL). Results are the mean ± SD of triplicates of two independent experiments. Treated samples were compared to untreated using Student's *t* test: ***$p < 0.001$.

50 μg/mL. All these nanoparticles hemolyzed human red blood cells in a range of 4.6% to 7% (in Figure 1), $KNbO_3$ HNPs being less hemolytic. For a comparison, HNPs were found to be less hemolytic than amorphous silica NPs,[31] their effect being comparable to that of mesoporous silica nanoparticles (MSN)[32] but more prominent than that observed for PEGylated MSN. This last finding suggests that a stable polymer coating of HNPs might decrease their hemolytic effect.

Multiphoton Imaging. One essential aspect of our study is to estimate the potential of HNPs for complementing fluorescent labels for defined applications including long-term cell tracking and deep tissue imaging by infrared excitation. In this respect, an essential comparison is to assess the contrast yielded by individual HNPs against a commonly used cell dye under different excitation conditions in a commercial multiphoton imaging platform. In Figure 2, a comparison of images obtained with the excitation laser set at 700 (A), 790 (B), 870 (C), and 970 (D) nm is reported. In the top panel, the different excitation spectra (A−D) are reported together with their corresponding second-harmonic peaks calculated on the basis of the experimental laser bandwidth (A′−D′). This plot also includes absorption (dotted line) and fluorescence (continuous line) bands of FM1-43FX cell membrane dye, which was used to stain HTB-182 lung cancer cells exposed for 24 h to PEG-stabilized $KNbO_3$ HNPs. The first image row displays the four detection channels overlaid, while in the second row only the relevant SH channel for each excitation wavelength is presented. To allow a quantitative comparison among these images, all the relevant laser parameters (pulse energy, peak power, focus) were kept constant. Likewise, the detection parameters (pixel dwell time, number of averaging, detector gain) and image processing were identical. Taking into account the photomultiplier's sensitivity and overall transmission of spectral filtering optics, the system detection efficiency varies less than a factor of 2 between the extreme wavelengths imaged (360 and 485 nm). One can notice how the HNPs can be easily retrieved at any excitation wavelength, and their narrow emission band can be easily separated from the

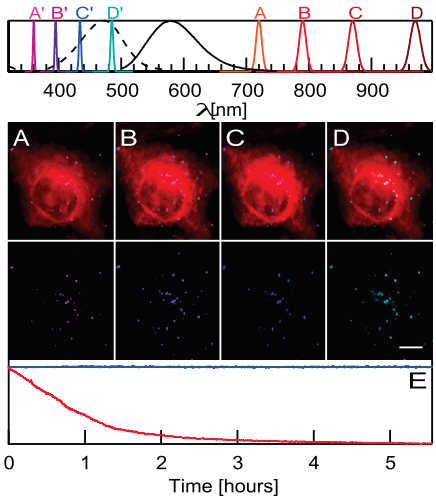

Figure 2. Excitation wavelength imaging comparison. Upper plot: Laser excitation (A, B, C, D) and corresponding calculated SH spectra (A′, B′, C′, D′). Absorption (dashed line) and fluorescence (continuous line) spectra of FM 1-43 cell membrane dye. First image row: Multiphoton images of HTB-182 cells exposed for 24 h to $KNbO_3$ with laser excitation set at 720 nm (A), 790 nm (B), 868 nm (C), and 970 nm (D). All detection channels overlaid. Second image row: Images obtained plotting only the relevant SH detection channel (A′, B′, C′, D′) for each excitation wavelength. The scale bar corresponds to 20 μm. Lower plot: Long-time behavior upon continuous laser irradiation of the simultaneously acquired signals from $KNbO_3$ HNPs (SH, blue) and from FM1-43FX (fluorescence, red) (E). **$p < 0.01$.

broad band fluorescence of a dye expressly chosen for its large absorption bandwidth. As we demonstrated in a previous work, the HNPs can be efficiently excited in the infrared spectral region (up to 1.5 μm and more[6]), minimizing two-photon-induced autofluorescence[33] and increasing imaging penetration depth due to the reduced scattering at longer wavelengths.[34]

The photostability of the particles' harmonic signal with respect to that of the FM1-43FX dye is striking, as one can appreciate from the comparison reported in Figure 2 E. Contrary to the exponential bleaching observed for fluorescence, the HNPs' response remains absolutely flat over hours of constant irradiation. Such long-term stability opens the way to the monitoring of labeled cellular structures evolving over days (stem cells, neural structures).

To complete this survey, we have carried out a systematic image screening over all the nanocrystals and cell lines, to identify specific trends or peculiarities related to the different nanomaterials and/or cellular samples. A representative result of this comprehensive study is reported in Figure 3, displaying BEAS-2B cells exposed for 5 h to PEG-stabilized $BaTiO_3$, $KNbO_3$, $LiNbO_3$, KTP, and ZnO HNPs at 50 μg/mL concentration. For the former three materials (panels A−C), one can observe a reasonable association to cells of the HNPs; the latter have the tendency to remain confined at the membranes (as confirmed by the slice views extracted from a z-stack in F), apart from a few individual

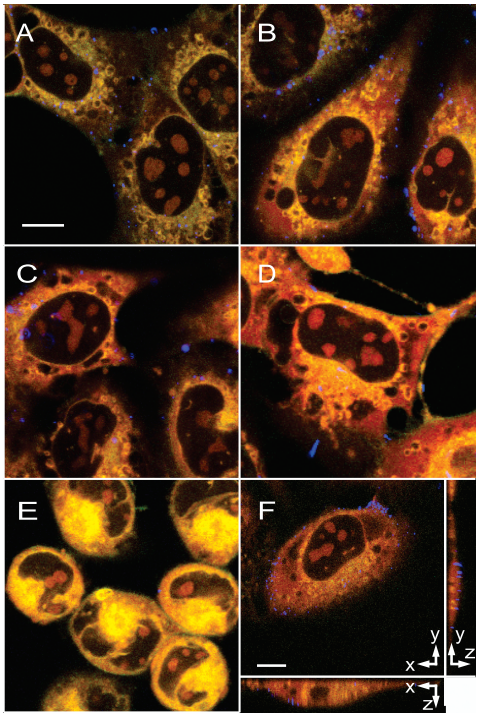

Figure 3. BEAS-2B cells exposed for 5 h to (A) $BaTiO_3$, (B) $KNbO_3$, (C) $LiNbO_3$, (D) KTP, and (E) ZnO HNPs. (F) Sliced views from a z-stack of cells exposed to $KNbO_3$ HNPs. The scale bars correspond to 10 μm.

exceptions of HNPs within the cytoplasm. This preferential association to the membranes is consistent with the short contact time, as it is known that uptake by endocytosis of solid core NPs typically takes place over longer times.[35,36] The cells look healthy, in agreement with the survival rate determined by MTT. The situation is different for KTP (panel D): in this case, the larger HNP size together with the growth of micrometric rod-shaped structures might be at the origin of the observed reduced particle uptake. Incidentally, we point out that the presence of such larger structures is consistent with the DLS measurement and can explain the poor reproducibility observed for KTP HNP stabilization. An extreme situation, again in complete agreement with the MTT results, is found for ZnO (panel E): there is almost no trace of HNPs on the sample, and the round shape of the cells is a clear sign of their poor health state. Such a high degree of toxicity has been recently ascribed to ZnO partial dissolution and induction of oxidative stress.[37] This explanation would be consistent with the absence of HNPs in our images.

CONCLUSIONS

We have tested in a rigorous way under the same experimental conditions the performance of five different nonlinear active nanomaterials to identify the best candidate for biological applications. The very properties related to the nonresonant nature of the HNP approach (wavelength flexibility, extreme photostability) do not depend on the chemical composition and are shared among all the samples. The optical characterization, performed both on ensemble (by HRS) and on individual HNPs (by multiphoton microscopy), indicates that the harmonic conversion efficiency can be readily related to that of the corresponding bulk materials and that the harmonic responses of the different samples are very similar. Moreover, for all samples tested, we observed an excellent optical contrast exerted by the HNPs with respect to a standard cell dye under normal imaging conditions. Very notably, the SH signal presents a flat response over hours of constant irradiation as opposed to fluorescence bleaching. Given the similarities of the nonlinear optical properties among the different nanomaterials, a sensible choice must be made according to other criteria including synthesis, stability, and biocompatibility. As discussed in Materials and Methods, we encountered several difficulties in various steps of the KTP and $BaTiO_3$ HNP preparation, which we attributed to the higher polydispersity of these samples. KTP HNPs feature also the largest average size among all the nanocrystals tested. Concerning biocompatibility, which remains the real point of comparison, to the best of our knowledge two of these materials have been already employed for SH cell labeling: ZnO HNPs[17,19] and $BaTiO_3$ HNPs,[14,17] which have also been recently used for a proof-of-principle *in vivo* application.[38] For the former, several authors reported high toxicity.[39,40] For the latter, on the other hand, two recent publications indicate high cytocompatibility.[41,42] In our work, HNP cytotoxicity was generally found acceptable also after long-time exposure. The only notable exception is again ZnO HNPs, which showed highly cytotoxic effects even after short contact times with the cells. The hemolytic potential, which would be an adverse occurrence for prospective clinical applications of HNPs, was found to be very weak for all nanomaterials under scrutiny. Finally, for a future use of HNPs in human context, further analyses are needed, specifically focused on their interactions with human blood and cell-derived components, to assess their biological behavior when coated by a protein corona.[43]

MATERIALS AND METHODS

Dispersion and Water Stabilization of Nanomaterials. $KNbO_3$ and $BaTiO_3$ NPs obtained by grinding of bulk crystals were freely provided by the company FEE GmbH (Idar-Oberstein, Germany); KTP raw powders, by the company Cristal Laser S.A. (Messein, France). ZnO NPs were purchased from Nanoamor (Houston, TX, USA): commercial nominal size 20 nm, 99.5% purity, 50 m^2/g specific surface area. Finally, $LiNbO_3$ powders were kindly supplied by the SRSMC laboratory (Nancy, France).[16] PEG (molecular weight 5000 g/mol, Sigma Aldrich) and all agglomerated nanopowders were used as received without further purification.

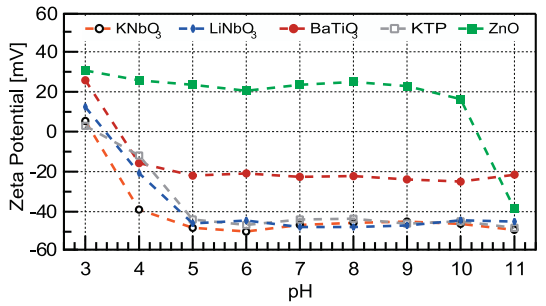

Figure 4. Zeta-potential variations as a function of pH of $KNbO_3$, $LiNbO_3$, $BaTiO_3$, KTP, and ZnO HNPs dispersed in water. Each data point results from the averaging of three independent measurements.

The protocol applied for colloidal suspensions is the following: (i) Nanopowders are first dispersed into deionized water with a typical concentration of 0.4 mg/mL. (ii) Dispersions are exposed to sonication for 25 min (Vibra Cell 75043, Bioblock Scientific) at a maximum input power of 750 W and at a frequency of 20 kHz. A pulsed irradiation (1 s on and 4 s off) at room temperature was found optimal for the preparation of homogeneous dispersions.[44] (iii) The pH of water dispersions is fixed at 7 for $LiNbO_3$, $KNbO_3$, KTP, and ZnO and 3 for $BaTiO_3$ to match with the stability regions (Figure 4) previously determined at fixed ionic strength for each nanomaterial by zeta-potential measurements (Zetasizer Nano ZS, Malvern Instruments Ltd.). (iv) Solutions are then left to settle during one to seven days to allow sedimentation of the larger particles and aggregates. Note that for each nanocrystal sedimentation kinetics was determined by time-dependent DLS measurements. (v) HNP concentration at the end of the sedimentation period is estimated by weighing the residual fraction (assuming spherically shaped NPs). It corresponds to 10−30% of the initial concentration according to the nanomaterial under consideration.

For biological evaluation, the colloidal stability of HNPs is improved by PEG adsorption. Various amounts of PEG were tested; in all cases a fixed concentration of 18 mg/mL was necessary to obtain stable zeta-potential values. Typically, 1 g of PEG was added to 55 mL of as-obtained supernatants. The colloidal suspensions were then left under smooth agitation for 15 min in a standard ultrasonic bath. PEG in excess was finally removed by centrifugation at 113000*g* for 90 min (Beckman L7-65 ultracentrifuge, Rotor SW28, Beckman centrifuge tube polycarbonate thick wall: capacity 38.5 mL). The absence of HNPs in supernatants after centrifugation was confirmed by DLS and HRS measurements. PEG-stabilized HNPs of mean DLS size 120−140 nm were then readily redispersed in deionized water at 1 mg/mL and at pH = 7.

Ensemble Optical Measurements. A commercial DLS apparatus was employed for evaluating size and particle-size distribution (Malvern Zetasizer NanoZS). For the HRS characterization, a YAG laser at 1064 nm (Wedge HB, Bright solutions, 1 mJ/1 ns) was focused by a 20 cm focal length lens into a glass cuvette. The scattered SH radiation was collected perpendicularly to the incident beam by a *f*/4 lens and detected by a photomultiplier coupled to a boxcar integrator. A colored glass filter (short pass) and an interferometric filter (532 nm) were placed in front of the photomultiplier to ensure that exclusively the SH intensity was accounted for.[22]

Cells. A549, HTB-178, HTB-182, and BEAS-2B cell lines are available from ATCC (American Tissue Culture Collection, Manassas, VA, USA). A549 and BEAS-2B cells were grown in Dulbecco's modified Eagle's medium (DMEM) containing 4.5 g/L glucose, 10% heat-inactivated fetal calf serum (FCS), and penicillin/streptomycin (all cell culture reagents were obtained from Invitrogen, Basel, Switzerland). HTB-178 cells were grown in complete Roswell Park Memorial Institute (RPMI) 1640 medium (Invitrogen) supplemented with 20% FCS and penicillin/streptomycin. HBT-182 cells were grown in RPMI 1640 medium supplemented with 10% FCS and penicillin/streptomycin.

Determination of Cytotoxicity. The cells were grown for 48 h in 48-well plates (250 μL/well) (Corning, NY, USA). Then the medium was changed, HNPs diluted in complete culture medium were added at the indicated concentrations, and cells were further incubated for different time periods (5, 24, 72 h). MTT from Sigma-Aldrich was diluted at 5 mg/mL in phosphate-buffered saline (PBS), and 10 μL per well was added for 2 h. Then, cell culture supernatants were removed, the cell layers were dissolved in 250 μL of 2-propanol/0.04 N HCl for 15 min, and 200 μL of the solutions was transferred into a 96-well plate (Corning). Absorbance at 540 nm was measured in a multiwell plate reader (iEMS Reader MF, Labsystems, Bioconcept, Allschwil, Switzerland) and compared to the values of control cells incubated only with the appropriate culture medium. Experiments were conducted in triplicate wells and repeated twice.

Evaluation of Microbial Contamination of the NPs. For the evaluation of microbial contamination, HNP stock solutions at 50 μg/mL in cell media were incubated for 24 h at 37 °C. Microbial contamination assays were performed by a private company (TIBIO, Comano, Switzerland) under a collaboration agreement. Samples were tested for the contamination of aerobic bacteria, facultative aerobic bacteria, and fungi.

Hemolysis Assay. Fresh human blood in lithium heparin-containing tubes (BD Falcon, Erembodegem, Belgium) was obtained from leftovers of analytical blood with normal values. The plasma was removed by centrifugation for 10 min at 2500 rpmi, and the blood cells were washed three times with sterile isotonic PBS, then diluted 1:10 in PBS. A 300 μL amount of the cell suspension was added to 1200 μL of each NP solution in PBS (final concentration of NPs: 50 μg/mL). Nanopure water (1200 μL) was used as a positive control, and PBS (1200 μL) was used as a negative control. The mixtures were gently mixed, then kept for 2 h at room temperature and centrifuged for 2 min at 4000 rpm. Finally, the absorbance of the upper solutions was measured at 540 nm in an absorbance multiwell plate reader (iEMS Reader MF). The hemolysis percentage of the samples was calculated by dividing the difference in absorbance between the samples and the negative control by the difference in absorbance between the positive and negative controls. Experiments were conducted in triplicate wells and repeated twice.

Sample Preparation for Multiphoton Imaging. Cells were grown for 24 h on round glass slides (12 mm diameter) in 24-well plates (Corning) (500 μL/well). HNPs diluted in fresh complete culture medium were added at the indicated concentrations, and cells were further incubated for the different time periods tested (5, 24, and 72 h). Then, cells were exposed to 5 μg/mL of FM1-43FX fluorescent probe (Invitrogen, 1 mg/mL stock solution in DMSO) for 1 min on ice, washed with PBS, and maintained in 4% buffered paraformaldehyde at 4 °C until image acquisition.

Multiphoton Imaging. The imaging setup is based on a Nikon A1R-MultiPhoton inverted microscope coupled with a Spectra-Physics Mai-Tai tunable oscillator (100 fs, 80 MHz, 700−1100 nm). Four independent non-descanned detectors acquire in parallel the epi-collected signal spectrally filtered by four tailored pairs of dichroic mirrors and interference filters, corresponding to 395 ± 5.5, 485 ± 10, 531 ± 20, and 607 ± 35 nm. For punctual measurements, we employed also two additional filters: 360 ± 6 and 434 ± 8.5 nm. For spectral excitation comparison, the laser mean power was kept constant at the different wavelength settings by monitoring it by a powermeter placed at the sample position. In order to maintain the same peak power across the Mai-Tai tunability range, the laser pulse precompressor was adjusted at every wavelength by maximizing the SH signal from individual HNPs dispersed on a substrate.

Conflict of Interest: The authors declare no competing financial interest.

Acknowledgment. This research has been conducted under the European FP7 Research Project NAMDIATREAM (NMP4-LA-2010-246479, http://www.namdiatream.eu). The authors are grateful to the SRSMC Laboratory in Nancy for supplying $LiNbO_3$ HNPs and for performing TEM and viscosity measurements. We are also grateful to Patrick Hole at Nanosight Ltd. (U.K.) for the nanoparticle tracking analysis.

Supporting Information Available: TEM images, DLS and FTIR spectra, and additional information on the calculation

procedure of the nonlinear coefficients are available free of charge *via* the Internet at http://pubs.acs.org.

REFERENCES AND NOTES

1. Willig, K. I.; Kellner, R. R.; Medda, R.; Hein, B.; Jakobs, S.; Hell, S. W. Nanoscale Resolution in GFP-Based Microscopy. *Nat. Methods* **2006**, *3*, 721–723.
2. Denk, W.; Strickler, J. H.; Webb, W. W. 2-Photon Laser Scanning Fluorescence Microscopy. *Science* **1990**, *248*, 73–76.
3. Wang, F.; Liu, X. G. Recent Advances in the Chemistry of Lanthanide-Doped Upconversion Nanocrystals. *Chem. Soc. Rev.* **2009**, *38*, 976–989.
4. Bonacina, L.; Mugnier, Y.; Courvoisier, F.; Le Dantec, R.; Extermann, J.; Lambert, Y.; Boutou, V.; Galez, C.; Wolf, J. P. Polar $Fe(IO_3)_3$ Nanocrystals as Local Probes for Nonlinear Microscopy. *Appl. Phys. B: Laser Opt.* **2007**, *87*, 399–403.
5. Le Xuan, L.; Zhou, C.; Slablab, A.; Chauvat, D.; Tard, C.; Perruchas, S.; Gacoin, T.; Villeval, P.; Roch, J. F. Photostable Second-Harmonic Generation from a Single $KTiOPO_4$ Nanocrystal for Nonlinear Microscopy. *Small* **2008**, *4*, 1332–1336.
6. Extermann, J.; Bonacina, L.; Cuna, E.; Kasparian, C.; Mugnier, Y.; Feurer, T.; Wolf, J. P. Nanodoublers as Deep Imaging Markers for Multi-Photon Microscopy. *Opt. Express* **2009**, *17*, 15342–15349.
7. Extermann, J.; Bejot, P.; Bonacina, L.; Mugnier, Y.; Le Dantec, R.; Mazingue, T.; Galez, C.; Wolf, J. P. An Inexpensive Nonlinear Medium for Intense Ultrabroadband Pulse Characterization. *Appl. Phys. B: Laser Opt.* **2009**, *97*, 537–540.
8. Brasselet, S.; Le Floc'h, V.; Treussart, F.; Roch, J. F.; Zyss, J.; Botzung-Appert, E.; Ibanez, A. *In Situ* Diagnostics of the Crystalline Nature of Single Organic Nanocrystals by Nonlinear Microscopy. *Phys. Rev. Lett.* **2004**, *92*, 207401.
9. Dutto, F.; Raillon, C.; Schenk, K.; Radenovic, A. Nonlinear Optical Response in Single Alkaline Niobate Nanowires. *Nano Lett.* **2011**, *11*, 2517–2521.
10. Le Xuan, L.; Brasselet, S.; Treussart, F.; Roch, J. F.; Marquier, F.; Chauvat, D.; Perruchas, S.; Tard, C.; Gacoin, T. Balanced Homodyne Detection of Second-Harmonic Generation from Isolated Subwavelength Emitters. *Appl. Phys. Lett.* **2006**, *89*, 121118.
11. Sandeau, N.; Le Xuan, L.; Chauvat, D.; Zhou, C.; Roch, J. F.; Brasselet, S. Defocused Imaging of Second Harmonic Generation from a Single Nanocrystal. *Opt. Express* **2007**, *15*, 16051–16060.
12. Extermann, J.; Bonacina, L.; Courvoisier, F.; Kiselev, D.; Mugnier, Y.; Le Dantec, R.; Galez, C.; Wolf, J. P. Nano-FROG: Frequency Resolved Optical Gating by a Nanometric Object. *Opt. Express* **2008**, *16*, 10405–10411.
13. Baumner, R.; Bonacina, L.; Enderlein, J.; Extermann, J.; Fricke-Begemann, T.; Marowsky, G.; Wolf, J. P. Evanescent-Field-Induced Second Harmonic Generation by Noncentrosymmetric Nanoparticles. *Opt. Express* **2010**, *18*, 23218–23225.
14. Hsieh, C. L.; Grange, R.; Pu, Y.; Psaltis, D. Three-Dimensional Harmonic Holographic Microcopy using Nanoparticles as Probes for Cell Imaging. *Opt. Express* **2009**, *17*, 2880–2891.
15. Nakayama, Y.; Pauzauskie, P. J.; Radenovic, A.; Onorato, R. M.; Saykally, R. J.; Liphardt, J.; Yang, P. D. Tunable Nanowire Nonlinear Optical Probe. *Nature* **2007**, *447*, 1098–U8.
16. Aufray, M.; Menuel, S.; Fort, Y.; Eschbach, J.; Rouxel, D.; Vincent, B. New Synthesis of Nanosized Niobium Oxides and Lithium Niobate Particles and their Characterization by XPS Analysis. *J. Nanosci. Nanotechnol.* **2009**, *9*, 4780–4785.
17. Pantazis, P.; Maloney, J.; Wu, D.; Fraser, S. E. Second Harmonic Generating (SHG) Nanoprobes for *in Vivo* Imaging. *Proc. Natl. Acad. Sci. U. S. A.* **2010**, *107*, 14535–14540.
18. Johnson, J. C.; Yan, H. Q.; Schaller, R. D.; Petersen, P. B.; Yang, P. D.; Saykally, R. J. Near-Field Imaging of Nonlinear Optical Mixing in Single Zinc Oxide Nanowires. *Nano Lett.* **2002**, *2*, 279–283.
19. Kachynski, A. V.; Kuzmin, A. N.; Nyk, M.; Roy, I.; Prasad, P. N. Zinc Oxide Nanocrystals for Nonresonant Nonlinear Optical Microscopy in Biology and Medicine. *J. Phys. Chem. C* **2008**, *112*, 10721–10724.
20. Liufu, S.; Xiao, H.; Li, Y. P. Investigation of PEG Adsorption on the Surface of Zinc Oxide Nanoparticles. *Powder Technol.* **2004**, *145*, 20–24.
21. Studart, A. R.; Amstad, E.; Gauckler, L. J. Colloidal Stabilization of Nanoparticles in Concentrated Suspensions. *Langmuir* **2007**, *23*, 1081–1090.
22. Le Dantec, R.; Mugnier, Y.; Djanta, G.; Bonacina, L.; Extermann, J.; Badie, L.; Joulaud, C.; Gerrmann, M.; Rytz, D.; Wolf, J. P.; *et al.* Ensemble and Individual Characterization of the Nonlinear Optical Properties of ZnO and $BaTiO_3$ Nanocrystals. *J. Phys. Chem. C* **2011**, *115*, 15140–15146.
23. Hendrickx, E.; Clays, K.; Persoons, A. Hyper-Rayleigh Scattering in Isotropic Solution. *Acc. Chem. Res.* **1998**, *31*, 675–683.
24. Shaviv, E.; Banin, U. Synergistic Effects on Second Harmonic Generation of Hybrid CdSe-Au Nanoparticles. *ACS Nano* **2010**, *4*, 1529–1538.
25. Rodriguez, E. V.; de Araujo, C. B.; Brito-Silva, A. M.; Ivanenko, V. I.; Lipovskii, A. A. Hyper-Rayleigh Scattering from $BaTiO_3$ and $PbTiO_3$ Nanocrystals. *Chem. Phys. Lett.* **2009**, *467*, 335–338.
26. Schnekenburger, J.; Kroll, A.; Pillukat, M. H.; Hahn, D. Current *in Vitro* Methods in Nanoparticle Risk Assessment: Limitations and Challenges. *Eur. J. Pharm. Biopharm.* **2009**, *72*, 370–377.
27. Hukkanen, J.; Lassila, A.; Paivarinta, K.; Valanne, S.; Sarpo, S.; Hakkola, J.; Pelkonen, O.; Raunio, H. Induction and Regulation of Xenobiotic-Metabolizing Cytochrome P450s in the Human A549 Lung Adenocarcinoma Cell Line. *Am. J. Respir. Cell. Mol. Biol.* **2000**, *22*, 360–366.
28. Hellmann, G. M.; Fields, W. R.; Doolittle, D. J. Gene Expression Profiling of Cultured Human Bronchial Epithelial and Lung Carcinoma Cells. *J. Toxicol. Sci.* **2001**, *61*, 154–163.
29. Yang, F.; Xiao, Z. Q.; Zhang, X. Z.; Li, C.; Zhang, P. F.; Li, M. Y.; Chen, Y.; Zhu, G. Q.; Sun, Y.; Liu, Y. F.; *et al.* Identification of Tumor Antigens in Human Lung Squamous Carcinoma by Serological Proteome Analysis. *J. Proteome Res.* **2007**, *6*, 751–758.
30. Nichols, W. K.; Terry, C. M.; Cutler, N. S.; Appleton, M. L.; Jesthi, P. K.; Yost, G. S. Oxidation at C-1 Controls the Cytotoxicity of 1,1-Dichloro-2,2-Bis(P-Chlorophenyl)-Ethane by Rabbit and Human Lung-Cells. *Drug Metab. Dispos.* **1995**, *23*, 595–599.
31. Slowing, I. I.; Wu, C. W.; Vivero-Escoto, J. L.; Lin, V. S. Mesoporous Silica Nanoparticles for Reducing Hemolytic Activity towards Mammalian Red Blood Cells. *Small* **2009**, *5*, 57–62.
32. He, Q.; Zhang, J.; Shi, J.; Zhu, Z.; Zhang, L.; Bu, W.; Guo, L.; Chen, Y. The Effect of PEGylation of Mesoporous Silica Nanoparticles on Nonspecific Binding of Serum Proteins and Cellular Responses. *Biomaterials* **2011**, *31*, 1085–1092.
33. Zipfel, W. R.; Williams, R. M.; Christie, R.; Nikitin, A. Y.; Hyman, B. T.; Webb, W. W. Live Tissue Intrinsic Emission Microscopy using Multiphoton-Excited Native Fluorescence and Second Harmonic Generation. *Proc. Natl. Acad. Sci. U. S. A.* **2003**, *100*, 7075–7080.
34. Helmchen, F.; Denk, W. Deep Tissue Two-Photon Microscopy. *Nat. Methods* **2005**, *2*, 932–940.
35. Cengelli, F.; Voinesco, F.; Juillerat-Jeanneret, L. Interaction of Cationic Ultrasmall Superparamagnetic Iron Oxide Nanoparticles with Human Melanoma Cells. *Nanomedicine* **2010**, *7*, 1075–1087.
36. Halamoda-Kenzaoui, B.; Chapuis-Bernasconi, C.; Hofmann, H.; Juillerat-Jeanneret, L. Evaluation of Uptake and Transport of Ultrasmall Superparamagnetic Iron Oxide Nanoparticles by Human Brain-Derived Endothelial Cells. *Nanomedicine* **2012**, *7*, 39–53.
37. Xia, T.; Kovochich, M.; Liong, M.; MaÃE†dler, L.; Gilbert, B.; Shi, H.; Yeh, J. I.; Zink, J. I.; Nel, A. E. Comparison of the

Mechanism of Toxicity of Zinc Oxide and Cerium Oxide Nanoparticles Based on Dissolution and Oxidative Stress Properties. *ACS Nano* **2008**, *2*, 2121–2134.
38. Grange, R.; Lanvin, T.; Hsieh, C. L.; Pu, Y.; Psaltis, D. Imaging with Second-Harmonic Radiation Probes in Living Tissue. *Biomed. Opt. Express* **2011**, *2*, 2532.
39. Yang, H.; Liu, C.; Yang, D. F.; Zhang, H. S.; Xi, Z. G. Comparative Study of Cytotoxicity, Oxidative Stress and Genotoxicity Induced by Four Typical Nanomaterials: the Role of Particle Size, Shape and Composition. *J. Appl. Toxicol.* **2009**, *29*, 69–78.
40. Huang, C. C.; Aronstam, R. S.; Chen, D. R.; Huang, Y. W. Oxidative Stress, Calcium Homeostasis, and Altered Gene Expression in Human Lung Epithelial Cells Exposed to ZnO Nanoparticles. *Toxicol. in Vitro* **2010**, *24*, 45–55.
41. Ciofani, G.; Danti, S.; D'Alessandro, D.; Moscato, S.; Petrin, M.; Menciassi, A. Barium Titanate Nanoparticles: Highly Cytocompatible Dispersions in Glycol-Chitosan and Doxorubicin Complexes for Cancer Therapy. *Nanoscale Res. Lett.* **2010**, *5*, 1093–1101.
42. Hsieh, C.-L.; Grange, R.; Pu, Y.; Psaltis, D. Characterization of the Cytotoxicity and Imaging Properties of Second-Harmonic Nanoparticles. *Proc. SPIE* **2010**, *7759*, 77590T–77590T-6.
43. Lundqvist, M.; Stigler, J.; Elia, G.; Lynch, I.; Cedervall, T.; Dawson, K. A. Nanoparticle Size and Surface Properties Determine the Protein Corona with Possible Implications for Biological Impact. *Proc. Natl. Acad. Sci. U. S. A.* **2008**, *105*, 14625–14270.
44. Nguyen, V. S.; Rouxel, D.; Hadji, R.; Vincent, B.; Fort, Y. Effect of Ultrasonication and Dispersion Stability on the Cluster Size of Alumina Nanoscale Particles in Aqueous Solutions. *Ultrason. Sonochem.* **2011**, *18*, 382–388.